Journal of Materials Chemistry A

Accepted Manuscript

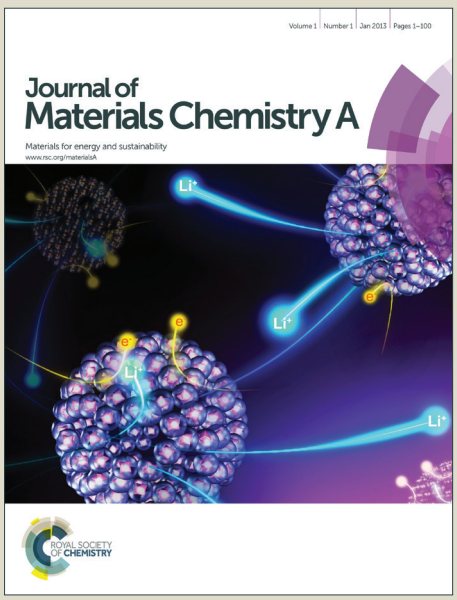

ROYAL SOCIETY OF CHEMISTRY

www.rsc.org/materialsA

July 3, 2014

J. Mater. Chem. A

Thermodynamic and kinetic assessments of strontium-doped lanthanum manganite perovskites for two-step thermochemical water splitting

Chih-Kai Yang[1], Yoshihiro Yamazaki[1,2]*, Aykut Aydin[1], and Sossina M. Haile[1]*

1 Materials Science, California Institute of Technology, Pasadena, CA 91125 USA
2 PRESTO, Japan Science and Technology Agency, Kawaguchi, 332-0012 Japan

* corresponding authors: yamazaki@caltech.edu, smhaile@caltech.edu

Abstract

Solar-driven thermochemical water splitting using non-stoichiometric oxides has emerged as an attractive technology for solar fuel production. The most widely considered oxide for this purpose is ceria, but the extreme temperatures required to achieve suitable levels of reduction introduce challenges in reactor design and operation, leading to efficiency penalties. Here, we provide a quantitative assessment of the thermodynamic and kinetic properties of $La_{1-x}Sr_xMnO_{3-\delta}$ perovskites, targeted for a reduced temperature operation of thermochemical water splitting. Sr-doping into lanthanum manganite increases the thermodynamic fuel production capacity, which reaches 9 ml g^{-1} for 0.4 Sr for a thermochemical cycle operated between 1400 and 800 °C. The hydrogen yields are moreover in good agreement with expected values based on analysis and extrapolation of thermogravimetric data available in the literature. High levels of Sr doping, however, result in low steam-to-hydrogen conversion rates, implying high energy penalties in an operational reactor. Furthermore, the rate of fuel production decreases with increasing Sr content, suggesting that intermediate compositions may yield the most suitable combination of properties.

July 3, 2014

1. Introduction

'Solar fuel' has emerged as a concept for storing the earth's vast solar resource in a high energy-density medium. Amongst many approaches currently pursued to generate solar fuels, thermochemical dissociation of water splitting is particularly attractive. It provides the benefits of full utilization of the solar spectrum as well as inherent temporal separation of hydrogen and oxygen gases.[1-3] Given these advantages, numerous multi-step cycles have been considered over the past several decades.[1, 2] Recently, two-step cycles making use of non-stoichiometric oxides have received attention because of the simplicity of their implementation.[4] The fuel production process operates on the basic thermodynamic principle that (partial) reduction of the oxide occurs at high temperature and reoxidation by steam (or carbon dioxide) occurs at low temperature. In such a process, solar-thermal heating releases oxygen from the bulk structure at high temperature, and the subsequent reaction with steam at lower temperature generates hydrogen. In the ideal case, both surface and bulk diffusion kinetics are rapid and thermodynamic equilibrium is quickly achieved in each half of the cycle. Accordingly, the ideal oxide demonstrates not only high sensitivity in oxygen content to environmental conditions, but also high oxygen diffusivity and high surface reaction constants. This set of characteristics is more commonly found in variable valence oxides, which can undergo partial reduction, than in those that undergo stoichiometric changes in oxygen content.[5]

Two classes of non-stoichiometric (variable valence) oxides have been evaluated for solar-driven thermochemical fuel production: fluorites based on ceria ($CeO_{2-\delta}$)[4-8] and perovskites based on lanthanum manganite ($LaMnO_{3-\delta}$, in which δ may be < 0)[9, 10] or on lanthanum aluminate ($LaAlO_3$)[11]. The relatively extensive studies of the ceria-based class of compounds has revealed that this group of materials generally requires rather high temperatures, > 1500 °C, to induce reduction of the oxide to an extent that the cycling yields non-trivial amounts of fuel.[5, 8] Such high temperatures, however, create significant challenges for reactor design and operation, although proof of principle has been successfully demonstrated with CeO_2.[4, 12] The perovskite class of materials has been considered explicitly for thermochemical cycling in just two recent experimental studies. McDaniel *et al.*[11] evaluated three compositions in the $Sr_xLa_{1-x}Mn_yAl_{1-y}O_{3-\delta}$ system using direct cycling and demonstrated high levels of fuel productivity for a high temperature reduction step of just 1350 °C. Scheffe *et al.*[10] carried out a more detailed evaluation of the potential of $La_{1-x}Sr_xMnO_{3-\delta}$ compounds (x = 0.2, 0.3, 0.4) for thermochemical fuel

production on the basis of literature data for the bulk thermodynamic redox properties and supplemented the analysis with an experimental study of the reduction behavior of the composition with $x = 0.35$. Although the fuel production half-cycle was not directly probed, the authors were able to show greater oxygen release from the perovskite than from ceria at moderate temperatures, indicating the potential for greater fuel productivity under reduced temperature cycling conditions. These authors further suggested, however, that obtaining high hydrogen yields would require large quantities of excess steam to drive the reaction to completion.[10] Prior to these studies of thermally driven CO_2 and H_2O dissociation, a handful of researchers have demonstrated CH_4 to syngas conversion over $La_{1-x}Sr_xMnO_{3-\delta}$.[13-15] This process also relies on the oxygen uptake and release of the oxide, however, the redox properties were not explicitly considered in these studies. In sum, these reports indicate that perovskite-structured materials have significant promise as reactive media for solar-driven thermochemical fuel production, but that the direct evaluation of this class of materials for this application is extremely limited. The present work has been carried out with the aim of providing a greater understanding of perovskite-structured oxides for solar fuels generation. We examine the $La_{1-x}Sr_xMnO_{3-\delta}$ system in particular because of the availability of thermogravimetric data. We complement an analytical evaluation of these materials with extensive thermochemical cycling experiments.

2. Background: Structural, thermodynamic and kinetic properties of $La_{1-x}Sr_xMnO_{3-\delta}$

Several structural distortions of the parent cubic perovskite structure have been reported for $La_{1-x}Sr_xMnO_{3-\delta}$, depending on the Sr concentration, oxygen partial pressure, and temperature, as determined most reliably by neutron powder diffraction.[16, 17] Near-stoichiometric $LaMnO_3$, in which the Mn has an average 3+ oxidation state, displays a Jahn-Teller distortion, and adopts an orthorhombic structure. Under typical processing conditions, the undoped composition contains oxygen excess and the accompanying high concentration of Mn^{4+} eliminates the distortion, resulting in a rhombohedral structure with space group $R\bar{3}c$. Introduction of Sr similarly generates a high concentration of Mn^{4+} under ambient conditions (rather than oxygen vacancies), resulting in the same rhombohedral structure. Very high concentrations of Sr ($x \geq 0.47$) lead to a tetragonal structure (*I4/mcm*) and ultimately a cubic structure ($Pm\bar{3}m$) beyond 0.7 Sr.[16, 17] The present studies are limited to $x = 0.4$, at which, under ambient conditions, the cubic phase is not

expected. In analogous cobaltite and ferrite perovskites, extreme reduction and the concomitant high concentration of vacancies can lead to the vacancy-ordered Brownmillerite phase.[18, 19] In the case of strontium-doped lanthanum manganite, this phase has been observed only upon reduction with hydrides or upon exposure to 50% hydrogen gas.[20, 21] Such extreme reducing conditions are not encountered under typical thermochemical cycling conditions and accordingly the Brownmillerite phase is not anticipated to form as part of the fuel generation process.

The thermodynamic capacity of an oxide for fuel production by thermochemical cycling is embedded in the reduction reaction

$$\frac{1}{\alpha}\mathrm{ABO}_{3-\delta} \leftrightarrow \frac{1}{\alpha}\mathrm{ABO}_{3-\delta-\alpha} + \frac{1}{2}\mathrm{O}_2(g) \quad (1)$$

where the designation of the oxide as an ABO_3 compound reflects the use of a perovskite, α represents an infinitesimal change in oxygen content, and the thermodynamic descriptors, the enthalpy and entropy of the reduction reaction, are recognized to be functions of nonstoichiometry, δ. Knowledge of the extent of this reaction for a given temperature (T) and oxygen partial pressure (pO_2) is equivalent to knowledge of the equilibrium dependence of δ on these environmental parameters.

Because of the technological importance of Sr-doped lanthanum manganites as cathodes for solid oxide fuel cells, experimental studies of the oxygen content of this class of materials at moderate temperatures and oxygen partial, typically up to ~ 1000 °C and in the range of 10^{-5} to 1 atm in oxygen partial pressure, as relevant for fuel cell technology, are available in the literature.[22-25] Extrapolation of these results for the prediction of oxygen content at the high temperatures of relevance for thermochemical cycling requires extraction of thermodynamic parameters from the raw experimental data. Most commonly, thermodynamic parameters are extracted with the goal of understanding defect chemistry and hence are concerned with the specifics of a defect model that can address, for example, possible defect association or clustering.[22, 26] While useful for meeting the objective of elaborating defect chemistry, such an analysis ultimately imposes some functional form for the dependence of enthalpy and entropy on δ, and discrepancies between the model and measured data can be anticipated to lead to large errors upon extrapolation to temperatures at which measurements were not performed.[10]

To address this challenge and provide robust predictions of fuel production capacity, we reevaluate the literature thermogravimetric data for strontium-doped lanthanum manganite using

an alternative approach that bypasses an interpretation of defect behavior and instead provides the enthalpy and entropy values for the reduction reaction as arbitrary functions of δ. In brief, as described by Panlener *et al.*,[27] the equilibrium constant for reaction (1) in the limit $\alpha \to 0$ is given by

$$K_{redox} = \left(pO_2^* \right)^{1/2} = \exp\left(-\frac{\Delta H^0_{redox} - T\Delta S^0_{redox}}{RT} \right) \quad (2)$$

where pO_2^* is the oxygen pressure relative to standard state, ΔH° and ΔS° are the standard enthalpy and entropy changes of the reduction reaction, respectively, and R is the universal gas constant. Rearranging this expression yields

$$\tfrac{1}{2} \ln pO_2^*\Big|_{\delta=\delta_0} = \frac{\Delta S^0_{redox}(\delta_0)}{R} - \frac{\Delta H^0_{redox}(\delta_0)}{RT} \quad (3)$$

Thus, if ΔH^0_{redox} and ΔS^0_{redox} are independent of temperature, an Arrhenius plot of the set of T and pO_2 that yield a given δ will appear as a straight line, with a slope that yields the enthalpy at that δ and an intercept that yields the entropy. Presuming the temperature independence of ΔH^0_{redox} and ΔS^0_{redox} holds at all temperatures (and no fundamental changes in material chemistry occur), $\Delta H^0_{redox}(\delta)$ and $\Delta S^0_{redox}(\delta)$ can be used to through an iterative treatment of Eq. (3) to determine δ under any condition.

Figures 1 and 2 show the results of this analysis using the thermogravimetric data reported by Misuzaki and coworkers for $La_{1-x}Sr_xMnO_{3-\delta}$ with x = 0 to 0.5.[22, 28] These are selected for analysis from the variety of datasets available in the literature because they span the widest range of temperatures (600-1000 °C) and widest number of compositions. As already noted in those authors' original report and reproduced here, Figure 1, the oxygen stoichiometry in $La_{1-x}Sr_xMnO_{3-\delta}$ is highly dependent on Sr content. In the absence of Sr, the material has a high concentration of excess oxygen ($\delta < 0$), believed to be charge and site balanced by cation vacancies (on both the A and B sites). With increasing Sr content, this oxygen excess region diminishes and, simultaneously, the oxygen deficient region enlarges. In the presence of Sr, charge balance is achieved either by an enhanced Mn^{4+} concentration or the presence of oxygen vacancies, the balance of which depends on T and pO_2.[22] Most significant for this discussion is

the observation that the computed values of oxygen content (dotted lines) are in good agreement with the experimental values (solid lines). This agreement provides confidence in the extracted $\Delta H^0_{redox}(\delta)$ and $\Delta S^0_{redox}(\delta)$ values, Figure 2, as well as the extrapolation of the oxygen nonstoichiometry values to high temperature.

Overlain on the data plots in Figure 1 are vertical lines corresponding to the values of oxygen partial pressure for the reduction and oxidation half-cycles employed in this work, 10^{-5} and 1.6×10^{-7} atm, respectively. Oxidation was performed at 800 °C using a gas stream of 20% H_2O in Ar. The equivalent oxygen chemical potential is computed assuming equilibrium for the thermolysis reaction, $H_2O(g) \leftrightarrow H_2(g) + 1/2O_2(g)$, and mass balance in the product generation (moles of H_2 = twice the moles of O_2). The equilibrium change in oxygen content, $\Delta\delta = \delta_f - \delta_i$, is indicated on these plots as the difference between oxygen content at the intersection of these respective vertical lines with the non-stoichiometry curves at 800 and 1400 °C. Excluding the undoped composition, it is evident that the greater the Sr content, the greater the expected change in oxygen content and hence fuel production. In the case of $LaMnO_{3-\delta}$, a contribution to $\Delta\delta$ appears due to the possibility of entering the oxygen excess region. Because accessing this nonstoichiometry would require significant atomic level structural rearrangements (cyclic generation and annihilation of cation vacancies), the undoped composition is not evaluated in this study.

The extracted thermodynamic functions, shown in Figure 2, also reveal important trends. Ignoring for the moment the oxygen excess region, a monotonic decrease in the enthalpy of reduction is evident with increasing Sr content, falling from ~ 350 kJ/mol-O for the undoped composition to ~ 230 kJ/mol-O for x = 0.5. In contrast, the entropy is relatively constant. This behavior directly reflects the fact that the material attains a higher oxygen deficiency with increasing Sr content at any given experimental condition of temperature and oxygen partial pressure and further reveals that the greater reducibility is due to a decrease in the enthalpy penalty of reduction rather than due to an increase in the entropy gain. A rough metric of reducibility is given by $T_{eq} = \Delta H^0_{redox}(\delta_0) / \Delta S^0_{redox}(\delta_0)$, which specifies the temperature at which a nonstoichiometry value of δ_0 would occur under a standard oxygen pressure of 1 atm. Again, the monotonic decrease in ΔH^0_{redox} with minimal change in ΔS^0_{redox} implies the reduction temperature monotonically decreases with Sr content. A second important observation from the results in

Figure 2 is the relative insensitivity, within the oxygen deficient region, of ΔH^0_{redox} to oxygen content. This is a feature of ideal solution behavior, in which the enthalpy of the reaction is independent of the number of defects. In such case, there is no apparent tendency towards either clustering or ordering of defects. Mizusaki *et al.* drew the same conclusion, that strontium-doped lanthanum manganite displays ideal solution behavior, from a more detailed analysis of the defect chemistry.[22] Within the oxygen deficient region one also sees that the enthalpy and entropy values of the manganite are substantially smaller than those of ceria,[27] considered a benchmark material for thermochemical fuel production. Because the enthalpy is particularly high for ceria, the temperatures required for reduction are higher than they are for strontium-doped lanthanum manganite. Indeed, the high enthalpy is the fundamental reason that thermochemical cycling with ceria must be carried out at extremely high temperatures.[5]

Both the enthalpy and entropy of reduction of $La_{1-x}Sr_xMnO_{3-\delta}$ undergo abrupt changes at the boundary between the oxygen deficient and oxygen excess regions, where the latter region is observed only in low Sr content compositions (undoped or 10 at% Sr). Given the substantially different means by which the structure accommodates excess oxygen from that in which it accommodates oxygen vacancies, such a result is not surprising. The enthalpy of reduction undergoes a particularly strong decrease in value, indicating that reduction occurs relatively easily for a material that has an excess of oxygen. Conversely, it implies that oxidizing the material with steam to utilize the oxygen excess capacity will be difficult. Anticipation of such behavior is another reason that the undoped material has not been experimentally evaluated in this study.

Turning from thermodynamic expectations to kinetic characteristics, the ideal reaction substrate for thermochemical cycling will display both rapid bulk diffusion and high surface reaction rates. Diffusion here refers to chemical (or ambipolar) diffusion of neutral oxygen species, a combination of ionic and electronic transport contributions. While several studies have been carried out using isotope exchange methods to probe oxygen self diffusion coefficient, D^*, and isotopic surface exchange rate, k^*,[29-33] surprisingly few have targeted direct measurements of chemical diffusivity, D_{chem} (or D^δ) and chemical surface exchange constant, k_S (or k^δ) under the driving force of a chemical potential gradient,[34-36] the kinetic parameters of relevance to thermochemical cycling. While it is possible, in principle, to transform between D^* and D_{chem}

and analogously between k^* and k_S using knowledge of the thermodynamic behavior of the material,[37] the discussion here focuses on the direct measurements of D_{chem} and k_S.

Yasuda *et al.*[35] determined D_{chem} for compositions in the range of x = 0.05 to 0.2 using the conductivity relaxation method, whereas Belzner *et al.*[34] determined D_{chem} for compositions with x = 0.2 and 0.5 using the potentiostatic step method. Yasuda's studies showed that at the low pO_2 values that could be probed by conductivity relaxation (10^{-10} – 10^{-17} atm, depending on temperature, over the range 850 to 1000 °C), the chemical diffusivity falls between 10^{-5} and 4×10^{-4} cm^2s^{-1}, decreases with increasing pO_2 (a linear dependence was observed on a double-logarithmic plot) and is insensitive to Sr content. More oxidizing conditions could not be examined because of the insensitivity of conductivity to changes in oxygen partial pressure above ~ 10^{-9} atm. Belzner *et al*. measured D_{chem} under somewhat more oxidizing conditions and at slightly lower temperatures. The two sets of results are in general, though not complete, agreement and indicate that the oxygen chemical diffusion at 800 °C during the oxidation half-cycle of thermochemical fuel production will likely be at least 10^{-8} cm^2s^{-1}. For a typical diffusion length, l, of ~ 3 μm, this diffusion coefficient implies a characteristic time ($\tau_{diff} = l^2/4D_{chem}$) of approximately 2 s, suggesting that diffusion is unlikely to be rate-limiting for the overall fuel production process.

An important difference between the conclusions of Belzner relative to those of Yasuda concerns the role of Sr content on the chemical diffusivity. As discussed by Belzner, D_{chem} can, under select conditions, have a significant dependence on partial pressure. The dependence is embodied in the expression

$$D_{chem} = D_{V_o} t_{el} \left(-\frac{1}{2} \frac{\partial \ln pO_2^*}{\partial \ln [V_O^{\bullet\bullet}]} \right) = D_{V_o} t_{el} \Lambda \qquad (4)$$

where D_{V_o} is the diffusivity of oxygen vacancies, t_{el} is the transference number of electronic species, and $[V_O^{\bullet\bullet}]$ is the fractional oxygen vacancy concentration (indicated according to Kroeger-Vink notation[38]). At the relatively low oxygen vacancy concentrations present in strontium-doped lanthanum manganite under moderately oxidizing conditions, both D_{V_o} and t_{el} are largely independent of $[V_O^{\bullet\bullet}]$, the latter being close to 1 throughout the experimental conditions, and both are effectively independent of pO_2. The term in parenthesis in Eq. (4),

named here Λ, is clearly dependent on pO_2. This quantity is related, but not identical, to the thermodynamic factor, Γ, defined formally as $d\ln a_O / d\ln c_O$, where a_O and c_O are, respectively, the activity and concentration of oxygen in the solid. Because the specific manner in which oxygen stoichiometry in $La_{1-x}Sr_xMnO_{3-\delta}$ depends on pO_2 is sensitive to Sr content (Figure 1), one can anticipate that D_{chem} will, in turn, also be sensitive to Sr content. Indeed, Belzner directly measured the thermodynamic factor and found that, at close to 1 atm pO_2, Γ was about an order of magnitude higher for $La_{0.8}Sr_{0.2}MnO_{3-\delta}$ than for $La_{0.5}Sr_{0.5}MnO_{3-\delta}$. The authors concluded that this enhancement was responsible for the observed order of magnitude difference in the diffusion coefficients between the two compositions. In the more limited compositional range examined by Yasuda, Sr = 5 to 20 at %, no significant dependence on doping level was observed. Although the Belzner result suggests the possibility of a systematic variation of D_{chem} with Sr content, particularly beyond Sr = 20 at %, even an order of magnitude reduction of the diffusivity, resulting in $\tau_{diff} \sim 20$ s, is unlikely to render diffusion the rate-limiting step in thermochemical fuel production.

Determination of the surface reaction constant in the $La_{1-x}Sr_xMnO_{3-\delta}$ system by the conductivity relaxation method are limited to Yasuda's evaluation $La_{0.8}Sr_{0.2}MnO_{3-\delta}$ under CO/CO_2 gas mixtures over the temperature range 850 to 1000 °C[35] and to Yan's study of $La_{0.7}Sr_{0.3}MnO_{3-\delta}$ under reduced oxygen pressure over the temperature range 610 to 920 °C[36]. While some intriguing results have been revealed by these studies (a strong dependence on pO_2 in the case of $La_{0.8}Sr_{0.2}MnO_{3-\delta}$ and a strong dependence on crystallographic orientation in the case of $La_{0.7}Sr_{0.3}MnO_{3-\delta}$), the differing experimental conditions precludes drawing conclusions about the role of Sr concentration on the surface reaction step. In contrast, many different compositions have been examined by isotopic exchange methods.[29-33]. While no single study provides a comprehensive comparison over a wide range of compositions, in general, the data suggest there is no systematic trend for the dependence of the surface exchange rate constant on Sr content. Furthermore, because the surface reaction constant can be expected to be extremely sensitive to the exact nature of the gaseous species,[39] and measurements have not been carried out under H_2O-containing atmospheres, it is not possible to provide a meaningful estimate of the characteristic time for a surface-reaction-limited fuel production half-cycle. Similarly, in the absence of very high temperature data, estimates of the characteristic time for the reduction half-cycle are premature.

3. Experimental methods

$La_{1-x}Sr_xMnO_{3-\delta}$ (x = 0.1, 0.2, 0.3, 0.4) powders were prepared by solid-state reaction. Stoichiometric quantities of La_2O_3 (Alfa Aesar, REacton®, 99.99%), $SrCO_3$ (Sigma-Aldrich ≥ 99.9%), and $MnCO_3$ (Sigma-Aldrich ≥ 99.9%) were combined and attritor-milled in isopropanol for 6 hours at 500 rpm. After drying, the powder was calcined at 1000 °C for 3 hours under air. A porous monolith was fabricated from this powder by mixing the latter with isopropanol (3 ml liquid per gram of powder) to obtain a thick paste. This paste was then placed (without application of pressure) into an alumina cylindrical mold with an inner diameter of 5 mm and fired at 1500 °C for 6 hours under air. The result was a loosely sintered, but mechanically rigid, porous body. The porosity was measured using mercury porosimetry (AutoPore IV, micromeritics) and the morphology examined by scanning electron microscopy (ZEISS 1550VP Field Emission SEM). Phase characterization was performed by X-ray powder diffraction (Panalytical, PW3040-PRO, Cu Kα radiation), for which the material was lightly hand-milled.

Thermochemical hydrogen production was carried out over a thermal cycle with reduction at 1400 °C and fuel generation at 800 °C. The sample was placed inside an alumina tube reactor in turn placed in infrared furnace with rapid heating and cooling capability. Temperature was measured with an S-type thermocouple placed in the axial center of the reactor and in contact with the porous pellet. The sample temperature was ramped to 1400 °C at 500 °Cmin^{-1} under flowing 10 ppm oxygen premixed with Ar (certified by Air Liquid), and held there for a given period of time (12-70 min, depending on composition) to observe oxygen release. At the end of the reduction step, the material was ramped down to 800 °C (also at 500 °Cmin^{-1}), and UHP Ar gas saturated with purified water at 60 °C (pH$_2$O = 0.20 atm, corresponding to pO$_2$ = 1.6 × 10^{-7} atm) was introduced. For the next reduction half-cycle, the gas was switched from H_2O-saturated argon to Ar (10 ppm O_2), and after a 3 min purge under this gas, the rapid heating from T_L (800 °C) to T_H (1400 °C) was initiated. Evolved oxygen and hydrogen gases were detected using mass spectroscopy (OMNI Star, Pfeiffer-vacuum). For quantitative determination of gas content, the ion current signal of the mass spectrometer was calibrated daily using 6 different hydrogen partial pressure ranging from 0 to 5.05×10^{-3} atm and 7 different oxygen partial pressure ranging from 1×10^{-5} to 3.83×10^{-3} atm.

4. Results and discussions

X-ray powder diffraction patterns of the as-synthesized $La_{1-x}Sr_xMnO_{3-\delta}$ and that of the material after thermochemical cycling (1400 °C/800 °C) are presented in Figure 3. Consistent with literature,[16, 17] all of the as-synthesized materials adopt the rhombohedral structure ($R\bar{3}c$). No structural changes were observed on cycling of materials with Sr content of 20 at% or higher. The 0.1 Sr sample, on the other hand, underwent a transformation from rhombohedral to orthorhombic, as revealed by the splitting of the peak at around 47° 2θ. This behavior reflects the fact that the fuel production step under 20 % steam at 800 °C presents a less oxidizing atmosphere than the original synthesis condition of laboratory air ($pO_2 \approx 0.2$ atm). Slight reduction of $La_{0.9}Sr_{0.1}MnO_{3-\delta}$ has been shown by Mitchell *et al.* to induce transformation to the orthorhombic phase, as a result of the previously described Jahn-Teller distortion.[12]

Secondary electron microscopy images, Figure 4, reveal a hierarchical structure in the porous monoliths, in which large (~ 60 μm) porous granules are formed from smaller sized crystallites or grains. The grain size decreases with increasing Sr content, from ~5 μm for 0.1 and 0.2 Sr to ~1 μm for 0.3 and 0.4 Sr. In contrast, the porosity (in as-synthesized samples) remains essentially constant with Sr content, Figure 5, with sample-to-sample variations more likely due to variations in fabrication steps rather than a systematic trend with composition. The large pores of these monoliths can be anticipated to be beneficial for ensuring gas transport through the porous body, whereas the small pores can be anticipated to ensure access to a large number of active sites at the surface. In addition, the finer structure of the high Sr content materials suggests enhanced kinetics may be observed for these materials due to the presumably higher specific surface area and the shorter solid-state diffusion length.

Typical oxygen release and hydrogen production profiles are presented in Figure 6a for $La_{0.8}Sr_{0.2}MnO_{3-\delta}$ (T_H = 1400 °C, atmosphere = 10 ppm O_2 in Ar; T_L = 800 °C, atmosphere = 20% H_2O in Ar). In this example, reduction and oxidation were carried out for 40 and 30 min, respectively. Oxygen is immediately released at the initiation of the heating step, whereas hydrogen is immediately produced upon introduction of steam at the low temperature step. The observation that strontium-doped lanthanum manganite can dissociate H_2O through a thermochemical process is fully consistent with the thermodynamic expectations. The data further reveal that the reduction reaches 90% of completion after 46 min, as determined from an evaluation of the peak decay behavior, whereas the oxidation reaches the same extent of

completion after just 6.2 min. Based on these observations, cycling experiments were performed using reduction and oxidation periods of 45 and 16 min, respectively. The results, Figure 6b, show relatively stable yields of both oxygen and hydrogen over 21 cycles.

In Figures 7 – 9 are shown the influence of Sr content on the thermochemical cycling behavior. The raw oxygen and hydrogen evolution profiles, Figure 7, reveal that the oxygen release and hydrogen production per cycle, on a per gram basis, increase with increasing Sr content, in general agreement with the thermodynamic expectations. Furthermore, the oxygen release kinetics, as roughly characterized by how quickly the gas evolution decays from its peak value, are largely unaffected by Sr content. The fuel production kinetics, in contrast, are strongly affected by Sr doping level, and even with a 65 min oxidation period, fuel production is clearly incomplete for the $x = 0.4$ composition. The difference in reduction and oxidation kinetics is further evident from an examination of the time required for the gas concentration to decrease to a value of 10% of the peak, Figure 8. In the case of oxygen release, the required time is just 1-2 minutes irrespective of oxide composition, whereas for hydrogen production it increases from about 1 min at $x = 0.1$ to almost an hour at $x = 0.4$. Possible origins of this kinetic behavior are considered below. The data cycling profiles presented in Figure 7(b) reflect oxidation half-cycle times that correspond to approximately 90% of reaction completion for the 'slow' compositions, for 0.3 and 0.4 Sr, as determined from evaluation of the profile decay behavior. While the reduction behavior appears, at first glance, to be rapid, particularly in comparison to these oxidation reactions, it is noteworthy that the oxygen release profiles are characterized by extremely long tails, not easily visible in Figure 7(a).

The cycling conditions of Figure 7 were repeated over multiple cycles as a means of evaluating stability and of gaining statistically averaged fuel production data. The per cycle oxygen and hydrogen yields for the $x = 0.2$ and 0.4 compositions (obtained from an integration of the area of the peak profiles) are presented in Figure 9. The error bars reflect the uncertainty in the integrated values due to background drift. Both materials show rather stable fuel productivity, indicating that, at least for thermal exposure periods of 22 and 15 h, respectively, morphological changes or mass losses from the material are negligible. Direct measurement of the sample mass after completion of the cycling experiments showed no more than 0.5% loss for all compositions. Accordingly, fuel productivity numbers quoted below are the averaged values over the multiple cycles. The cycling data further reveal that the H_2:O_2 molar ratio is within experimental error of

the theoretical value of 2, for 0.2 Sr, indicating that all oxygen vacancies created during reduction are consumed for fuel production during oxidation. In contrast, for 0.4 Sr, the ratio is consistently slightly less than 2, a result also obtained for the remaining two compositions. Such behavior may reflect incomplete oxidation by steam at 800 °C which is followed by oxidation by Ar/O_2 at 800 °C prior to high temperature reduction. In this way, the oxygen released on heating can exceed the corresponding production of hydrogen from reaction with steam. In addition, loss of hydrogen due to leaks is a ubiquitous challenge and can also account for some of the deviation. Loss of hydrogen relative to oxygen due to inherent material behavior, for example, inaccessibility of vacancies due to ordering, would be expected to be cumulative (with a declining per cycle hydrogen and oxygen productivity), and the stable behavior argues against any such interpretation.

A summary of the fuel production capacity of $La_{1-x}Sr_xMnO_{3-\delta}$ is provided in Table 1. Reported are the cycle-averaged measured values of oxygen and hydrogen production, as well as the projected quantity of oxygen release had long reduction times, sufficient to reach equilibrium, been employed. These projections are computed on the basis of the profile decay behavior and are provided along with estimates of the time required to reach equilibrium, again, based on the profile decay behavior. The projected values are useful for comparison against the values estimated from an analysis of the thermogravimetric data, as the latter are also representative of equilibrium behavior. Beyond the monotonic increase in fuel productivity with increasing Sr content already revealed in the raw profiles, it is evident from Table 1 that the projected oxygen release (and hence fuel productivity) is in excellent agreement with the thermodynamic predictions. The finite timescale of the measurements implies only a small penalty of about 10% on the fuel productivity. However, accessing that final 10% would require substantial increases in the total cycle time, as much as a factor of three in the case of $La_{0.6}Sr_{0.4}MnO_{3-\delta}$. The experimental hydrogen yields are 0.91, 2.89, 5.68 and 8.91 mlg^{-1}, respectively, for the four compositions. The latter two values are favorable in comparison to ceria, which has a hydrogen production capacity of 3.6 mlg^{-1} under comparable cycling conditions.[27]

While equilibrium fuel productivity provides one measure of the suitability of a material for thermochemical cycling, it has the potential to be misleading because it does not account for steam to hydrogen conversion efficacy. That is, an oxide that requires a small amount of steam to reach full reoxidation will be preferable to that which requires a large amount as the former will

inherently result in higher conversion rates, behavior that will ultimately benefit system efficiency. An estimate of the number of moles of water required to induce a given change in oxygen content in the oxides studied here is presented in Figure 10. The reduction is taken to reach equilibrium under an oxygen partial pressure of 10^{-5} atm and temperature of 1400 °C. This condition fixes the δ_i for each composition. The subsequent oxidation is taken to occur in a closed volume of variable size that allows equilibration between the oxide and the gas phase under an initial condition of 0.2 atm of H_2O partial pressure ($pO_2 = 1.6 \times 10^{-7}$ atm) and a temperature of 800 °C. The amount of fuel produced corresponds to $\Delta\delta$ and must, on thermodynamic grounds, increase with increasing steam input. The maximum $\Delta\delta$ possible occurs when δ_f reaches the equilibrium non-stoichiometry under $pO_2 = 1.6 \times 10^{-7}$ atm. The latter is close to 0 (Figure 1), and thus $\Delta\delta_{max}$ is just less than δ_i. The precise value of $\Delta\delta_{max}$ is unknown, however, as indicated by the large uncertainties given in the final column entry in Table 1, due to the challenges of measuring small weight changes with pO_2 as occurs in the vicinity of $\delta = 0$.

The results show that the steam requirement for fuel production from strontium-doped lanthanum manganite is rather high. For example, to achieve a $\Delta\delta$ of 0.02, possible only when x in $La_{1-x}Sr_xMnO_{3-\delta}$ is 0.3 or higher, requires a steam input ranging from about 1 to 1 moles H_2O per mole of oxide. This reactant input requirement in turn implies a steam-to-hydrogen conversion rate in the range of 2 to 4%. While this calculation corresponds to a worst case scenario and in a real, flowing system the influx of fresh reactant with high oxidizing power will decrease the steam requirement, the results show a clear composition trend. Specifically, the steam requirement increases with Sr content for a given $\Delta\delta$, yet, conversely, as already discussed, the fuel production capacity ($\Delta\delta_{max}$) also increases. The steam requirement for lanthanum strontium manganite, irrespective of specific composition, is also substantially greater than that when ceria is employed, computed here for comparison.[27] For example, δ_i for ceria is 0.031, and attaining a $\Delta\delta$ of 0.02 from this material (at the relatively unfavorable reduction temperature of 1400 °C) would require introduction of only slightly more than 0.02 moles of H_2O per mole of oxide, corresponding to almost a 100% steam-to-hydrogen conversion rate.

In general, the amount of steam required to achieve a target amount of hydrogen production approaches infinity as $\Delta\delta$ approaches $\Delta\delta_{max}$ (limitations of the raw thermogravimetric data in the region of $\delta = 0$ slightly obscure this behavior of $La_{1-x}Sr_xMnO_{3-\delta}$), indicating that efficient fuel production strategies may not be those that attain maximum fuel output per cycle.

Instead, cycling that forgoes the final stages of oxidation and hence limits the steam input may be preferable. For example, doubling the fuel output from $La_{0.6}Sr_{0.4}MnO_{3-\delta}$ from a $\Delta\delta$ of 0.05 to 0.1 would require about an order of magnitude increase in steam input. While it is impossible to achieve such high levels of fuel productivity from ceria (under the specified cycling atmospheres the maximum $\Delta\delta$ is 0.031), one must carefully weigh the tradeoffs between increased fuel production per formula unit of oxide versus the anticipated efficiency penalties of decreased conversion values before concluding which is the superior choice. Scheffe *et al.* recognized the need to operate strontium-doped lanthanum manganites under high steam input conditions and computed favorable solar-to-fuel conversion efficiencies from these perovskites under the assumption of 100% heat recovery from this large excess of steam.[10]

The kinetic characteristics of the $La_{1-x}Sr_xMnO_{3-\delta}$ materials for thermochemical fuel production merit further discussion. As already indicated in Figure 8, the time-scales associated with reduction are much shorter than those associated with oxidation. Moreover, the time to reach the peak in the oxygen release profile is approximately 1.1 min from the first detection of oxygen above the background level, a value that is unchanged with x. This time period is comparable to the 1.2 min required to heat the oxide from 800 to 1400 °C at the heating rate of 500 °Cmin^{-1}. From these observations, we conclude that, during the thermal reduction, each of the strontium-doped lanthanum manganites largely maintains an oxygen content that is equilibrated with its T and the gas phase pO_2. The long tail in the oxygen release profiles (present for each of the compositions) may reflect the decrease in the thermodynamic driving force as the oxygen chemical potential of the solid phase approaches that of the gas phase.

In contrast to oxygen release, fuel production is not only sluggish, but also sensitive to Sr content, Figure 8. Possible explanations for this include a systematic variation in morphological features, a decrease in chemical diffusivity, or a decrease in the surface reaction constant with increasing Sr doping level. From the SEM images, Figure 4, the decreasing grain size with increasing Sr content suggests a morphology that favors rapid reaction at large x. Given the observation of a characteristic time that increases with increasing Sr doping level, the morphological variations can be ruled out as the source of the differing kinetic responses. The chemical diffusivity, as noted, above can be expected to be dependent on Sr content as a result of the differing $\delta(pO_2,T)$ functional forms for the different compositions. As given in Eq. (4), D_{chem} is directly proportional to the quantity Λ, defined as

$$\Lambda = -\frac{1}{2}\frac{\partial \ln pO_2^*}{\partial \ln[V_O^{\bullet\bullet}]} \quad (5)$$

with the other terms, D_{V_O} and t_{el} being largely independent of oxygen partial pressure and composition over the experimental conditions considered. The computed values at 800 °C, Figure 11, show that Λ indeed varies with doping level. The value of this parameter at an internal oxygen chemical potential corresponding to a quench from 1400 °C is shown. Although Λ varies with Sr content, as with the morphological variations, the trend is the opposite of that required to explain the trend in hydrogen production kinetics. Furthermore, as already discussed, the absolute value of D_{chem} reported by both Yasuda *et al.* and by Belzner *et al.* implies a characteristic time that is far shorter than the times represented in Figure 8. Thus, diffusion can be ruled out as either the rate-limiting step or the source of the differing fuel production kinetics.

With morphology and bulk diffusivity eliminated, we turn to the surface reaction step. It is common to express the flux, specifically in this case the oxygen flux, J_O, across a surface at which a reaction occurs as

$$J_O = -k_{surf}\Delta C_O \quad (6)$$

where k_{surf} is the surface reaction rate constant, ΔC_O [$= C_{O,solid}(\text{interface}) - C_{O,gas}(\text{interface})$] is the difference in oxygen concentration across the solid-gas interface, and the reaction is taken to be first order with a rate constant that is independent of concentration. The expression above takes the driving force for the reaction to be the difference in concentration, but thermodynamic principles dictate that the driving force is, in fact, the difference in oxygen chemical potential $\Delta\mu_O = \mu_{O,solid}(\text{interface}) - \mu_{O,gas}(\text{interface})$. At the initiation of the hydrogen production step, these differences, ΔC_O and $\Delta\mu_O$, can be obtained directly from the oxygen non-stoichiometry curves, Figure 1. The ΔC_O values are essentially given by the $\Delta\delta$ values indicated between oxidizing and reducing conditions (also corresponding to $\Delta\delta_{max}$ described above). Recognizing that $\mu_O = \mu_O^0 + RT \ln pO_2$, the $\Delta\mu_O$ values correspond to the difference in effective oxygen partial pressures between the quenched state at 800 °C and the oxidized state at the same temperature.

The correlation between the peak in the hydrogen evolution and two parameters, $\Delta\delta$ (directly proportional to ΔC_O) and $\Delta\mu_O$, is shown in Figure 12. In the case of $\Delta\delta$, an anticorrelation is observed, with the peak generally decreasing in intensity with increasing concentration difference. In contrast, the peak height appears to be positively correlated with the magnitude of $\Delta\mu_O$. In both cases, the behavior of $La_{0.8}Sr_{0.2}MnO_{3-\delta}$ is somewhat anomalous. Ignoring this outlier, these results (in combination with the conclusion that diffusion cannot be rate-limiting) suggest that the hydrogen production half-cycle is surface reaction limited, and that the rate limitation arises from differences in the thermodynamic driving force for the reaction. It is of some value to note that, because the magnitude of $\mu_{O,gas}(\text{interface})$ is fixed by the reactor conditions (irrespective of the nature of the reactive oxide), $\Delta\mu_O$ directly scales with $\mu_{O,solid}(\text{interface})$. The latter is a measure of the oxygen chemical potential in the material upon quenching and, in turn, directly scales with ΔH_{redox}, suggesting that materials with small enthalpies of oxidation will be at a kinetic disadvantage relative to those with large enthalpies. On the other hand, in the absence of direct measurements of the surface reaction constant, it is premature to rule out a possible dependence of k_{surf} on Sr doping level as the cause of the depression in kinetics with increasing Sr content. Such behavior could arise indirectly from a dependence of k_{surf} on the (initial) bulk oxygen vacancy concentration, which increases monotonically with Sr content for the cycling conditions explored (Figure 1). Regardless of these possibilities (reduction of the driving force or inherent variation in k_{surf}), the elimination of diffusion as the rate-limiting step points towards a surface reaction limited process.

5. Conclusions

Thermodynamic and kinetic properties of Sr-doped lanthanum manganites, $La_{1-x}Sr_xMnO_{3-\delta}$ up to $x = 0.4$, were assessed for two-step thermochemical water dissociation. Existing thermogravimetric data were analyzed without reference to a specific defect chemical model to obtain generic values of the enthalpy and entropy of the reduction reaction as functions of nonstoichiometry. The equilibrium fuel productivity expected from thermochemical cycling between 800 and 1400 °C was computed using these extracted thermodynamic functions. Sr-doping was shown to increase the expected fuel productivity monotonically, reaching 8.9 ml

H_2/ml per cycle for $x = 0.4$. Oxygen evolution and hydrogen generation from steam were then experimentally confirmed. The materials exhibited stable fuel production over multiple cycles, with hydrogen productivities approaching the thermodynamically predicted values and hydrogen to oxygen production ratios close to the expected value of 2. Although Sr-doping lowers the amount of oxide required to produce 1 mole of hydrogen, it increases the amount of steam required. The kinetics of oxygen release on heating were found to be largely limited by the rate of temperature change of the material for heating rates of ~ 500 °C/min. In contrast, the fuel production kinetics were slower than could be explained by bulk (solid-state) mass diffusion limitations, indicating a surface reaction limited process. The rate was further found to decrease with increasing Sr content, possibly due to a decrease in the thermodynamic driving force for oxidation of the oxide with increasing dopant amount.

In sum, it is apparent there is a subtle trade-off between material characteristics in selecting the optimal material for solar-driven thermochemical fuel production. While lanthanum strontium manganite generates more fuel per cycle for reduced temperature cycling than ceria, this benefit comes at the price of increased steam requirements. In addition, within the $La_{1-x}Sr_xMnO_{3-\delta}$ system, the increase in fuel productivity with x comes at the price of a reduction in fuel generation kinetics. Thus, one can expect that the optimal material will be dependent on the cycling conditions, the details of the reactor and success in designing systems that provide high levels of gas phase heat recovery. Although these tradeoffs do not permit clear designation of $La_{1-x}Sr_xMnO_{3-\delta}$ as a superior material relative to ceria, it is to be recognized that, in contrast to the fluorite structure, the perovskite structure is host to an immense combination of elements. Thus, the potential for uncovering a perovskite composition with superb thermodynamic and kinetic characteristics for solar-driven thermochemical can be considered high.

Acknowledgements

This work was supported by the Precursory Research for Embryonic Science and Technology (PRESTO), Japan Science Technology Agency. We thank Prof. William Chueh for fruitful discussions and Mr. Stephen Wilke for performing mercury porosimetry measurements. We are further grateful to Prof. Yong Hao for assistance with the preparation of porous samples.

References

1. A. Steinfeld, *Solar Energy*, 2005, **78**, 603-615.
2. T. Kodama and N. Gokon, *Chemical Reviews*, 2007, **107**, 4048-4077.
3. J. E. Miller, M. D. Allendorf, R. B. Diver, L. R. Evans, N. P. Siegel and J. N. Stuecker, *Journal of Materials Science*, 2008, **43**, 4714-4728.
4. W. C. Chueh, C. Falter, M. Abbott, D. Scipio, P. Furler, S. M. Haile and A. Steinfeld, *Science*, 2010, **330**, 1797-1801.
5. W. C. Chueh and S. M. Haile, *Philos T R Soc A*, 2010, **368**, 3269-3294.
6. W. C. Chueh and S. M. Haile, *Chemsuschem*, 2009, **2**, 735-739.
7. M. Kang, X. M. Wu, J. Zhang, N. Zhao, W. Wei and Y. H. Sun, *Rsc Adv*, 2014, **4**, 5583-5590.
8. J. R. Scheffe, R. Jacot, G. R. Patzke and A. Steinfeld, *Journal of Physical Chemistry C*, 2013, **117**, 24104-24114.
9. *USA Pat.,* 2012.
10. J. R. Scheffe, D. Weibel and A. Steinfeld, *Energy and Fuels*, 2013, **27**, 4250-4257.
11. A. H. McDaniel, E. C. Miller, D. Arifin, A. Ambrosini, E. N. Coker, R. O'Hayre, W. C. Chueh and J. H. Tong, *Energ Environ Sci*, 2013, **6**, 2424-2428.
12. P. Furler, J. Scheffe, M. Gorbar, L. Moes, U. Vogt and A. Steinfeld, *Energy & Fuels*, 2012, **26**, 7051-7059.
13. A. Evdou, L. Nalbandian and V. T. Zaspalis, *Journal of Membrane Science*, 2008, **325**, 704-711.
14. A. Evdou, V. Zaspalis and L. Nalbandian, *International Journal of Hydrogen Energy*, 2008, **33**, 5554-5562.
15. L. Nalbandian, A. Evdou and V. Zaspalis, *International Journal of Hydrogen Energy*, 2009, **34**, 7162-7172.
16. J. F. Mitchell, D. N. Argyriou, C. D. Potter, D. G. Hinks, J. D. Jorgensen and S. D. Bader, *Physical Review B*, 1996, **54**, 6172-6183.
17. O. Chmaissem, B. Dabrowski, S. Kolesnik, J. Mais, J. D. Jorgensen and S. Short, *Physical Review B*, 2003, **67**, Artn 094431.
18. J. Ovenstone, J. S. White and S. T. Misture, *Journal of Power Sources*, 2008, **181**, 56-61.
19. I. A. Leonidov, V. L. Kozhevnikov, M. V. Patrakeev, E. B. Mitberg and K. R. Poeppelmeier, *Solid State Ionics*, 2001, **144**, 361-369.
20. R. Cortes-Gil, M. Hernando, M. L. Ruiz-Gonzalez, E. Cespedes, C. Prieto, J. M. Alonso, M. Vallet-Regi, A. Hernando and J. M. Gonzalez-Calbet, *Chemistry-a European Journal*, 2008, **14**, 9038-9045.
21. T. G. Parsons, H. D'Hondt, J. Hadermann and M. A. Hayward, *Chemistry of Materials*, 2009, **21**, 5527-5538.
22. J. Mizusaki, N. Mori, H. Takai, Y. Yonemura, H. Minamiue, H. Tagawa, M. Dokiya, H. Inaba, K. Naraya, T. Sasamoto and T. Hashimoto, *Solid State Ionics*, 2000, **129**, 163-177.
23. J. Mizusaki, Y. Yonemura, H. Kamata, K. Ohyama, N. Mori, H. Takai, H. Tagawa, M. Dokiya, K. Naraya, T. Sasamoto, H. Inaba and T. Hashimoto, *Solid State Ionics*, 2000, **132**, 167-180.
24. J. H. Kuo, H. U. Anderson and D. M. Sparlin, *Journal of Solid State Chemistry*, 1989, **83**, 52-60.
25. M. Andrieux and C. Picard, *Journal of Materials Science Letters*, 2000, **19**, 695-697.
26. J. Nowotny and M. Rekas, *Journal of the American Ceramic Society*, 1998, **81**, 67-80.
27. R. J. Panlener, R. N. Blumenthal and J. E. Garnier, *Journal of Physics and Chemistry of Solids*, 1975, **36**, 1213-1222.
28. J. Mizusaki, N. Mori, H. Takai, Y. Yonemura, H. Minamiue, H. Tagawa, M. Dokiya, H. Inaba, K. Naraya, T. Sasamoto and T. Hashimoto, personal communication.

29. S. Carter, A. Selcuk, R. J. Chater, J. Kajda, J. A. Kilner and B. C. H. Steele, *Solid State Ionics*, 1992, **53-6**, 597-605.
30. R. A. De Souza and J. A. Kilner, *Solid State Ionics*, 1998, **106**, 175-187.
31. R. A. De Souza, J. A. Kilner and J. F. Walker, *Materials Letters*, 2000, **43**, 43-52.
32. S. P. Jiang, *Journal of Materials Science*, 2008, **43**, 6799-6833.
33. S. Fearn, J. C. H. Rossiny, J. A. Kilner and J. R. G. Evans, *Solid State Ionics*, 2012, **211**, 51-57.
34. A. Belzner, T. M. Gur and R. A. Huggins, *Solid State Ionics*, 1992, **57**, 327-337.
35. I. Yasuda and M. Hishinuma, *Journal of Solid State Chemistry*, 1996, **123**, 382-390.
36. L. Yan, K. R. Balasubramaniam, S. L. Wang, H. Du and P. A. Salvador, *Solid State Ionics*, 2011, **194**, 9-16.
37. J. Maier, *Physical Chemistry of Ionic Materials*, John Wiley & Sons, Ltd, 2005.
38. F. A. Kroger and H. J. Vink, Academic Press, New York, 1956.
39. C. B. Gopal and S. M. Haile, *J Mater Chem A*, 2014, **2**, 2405-2417.

Figure Captions

Figure 1. Oxygen content in $La_{1-x}Sr_xMnO_{3-\delta}$ for several different values of x, as indicated. Solid blue lines are the experimental data for Mizusaki and co-workers,[22,23,28] collected for the temperature range from 600 to 1000 °C. High temperature experimental data for the $x = 0.35$ composition[10] are shown on the $x = 0.4$ plot as solid black dots. Dotted lines are fit and/or extrapolated values, derived as described in the text. Red dotted lines refer to extrapolated behavior at 1400 °C, at which reduction was carried in the present thermochemical cycling experiments. Green dotted lines refer to fit data at 800 °C, at which oxidation was performed. Open red and green circles indicate, respectively, expected values of oxygen content upon reduction under 10 ppm O_2 and oxidation under 20% H_2O. The difference in oxygen content between these open circles corresponds to $\Delta\delta_{max}$ shown in Figure 10.

Figure 2. Thermodynamic characteristics of the reduction of $La_{1-x}Sr_xMnO_{3-\delta}$: a) enthalpy and b) entropy of reduction as functions of oxygen non-stoichiometry; data for undoped ceria[27] shown for comparison.

Figure 3. X-ray powder diffraction patterns of $La_{1-x}Sr_xMnO_{3-\delta}$ before and after thermochemical cycling between 800-1400 °C: a) wider range and b) narrower range showing phase change from rhombohedral ($R\bar{3}c$) to orthorhombic (*Pbnm*) in $La_{0.9}Sr_{0.1}MnO_{3-\delta}$ after cycling. Dashed lines in a) indicate the region shown in b).

Figure 4. Microstructure of $La_{1-x}Sr_xMnO_{3-\delta}$ before thermochemical cycle between 800-1400 °C: a) typical porous structure for $x = 0.2$, b) impact of strontium content on grain size.

Figure 5. Porosity of $La_{1-x}Sr_xMnO_{3-\delta}$ as a function of strontium content before thermochemical cycle.

Figure 6. Thermochemical cycle of 1400 – 800 °C using $La_{0.8}Sr_{0.2}MnO_{3-\delta}$: a) typical cycle between high temperature dry state and low temperature wet state for 40 min in each step, b) 21 continuous cycles for thermochemical water splitting. Red and blue colors correspond to oxygen and hydrogen evolution, respectively. The high-temperature reduction and low-temperature oxidation steps were hold for 47 and 16 min, respectively.

Figure 7. Impact of strontium substitution in $La_{1-x}Sr_xMnO_{3-\delta}$ on thermochemical water splitting during 1400 – 800 °C cycle: a) oxygen evolution at 1400 °C, b) hydrogen evolution at 800 °C. The reduction time for 0.1, 0.2, 0.3 and 0.4 Sr at 1400 °C were 12, 47, 60 and 70 min, respectively, while the oxidation time at 800 °C were 8, 16, 36 and 65 min, respectively.

Figure 8. Characteristic hydrogen production and oxygen release times as functions of Sr content. Characteristic time is defined as that required for the off-gas detection to fall to 10% of the peak value.

Figure 9. Hydrogen and oxygen yield in $La_{1-x}Sr_xMnO_{3-\delta}$: a) $x = 0.2$ and b) $x = 0.4$. Reproducible hydrogen (blue) and oxygen (red) evolution over 21 and 8 cycles was observed in 0.2 and 0.4 Sr pellets, respectively. The reduction and oxidation times for 0.2 Sr were 47 and 16 min, respectively, whereas those for 0.4 Sr were 70 and 65 min, respectively. Uncertainty is estimated from the signal drift as observed during calibration. Where omitted, error bars lie within the data symbol.

Figure 10. Moles of water vapor required to induce the indicated stoichiometry change per mole of oxide at 800 °C using an input gas stream with $pH_2O = 0.2$ atm (balance inert), after reduction at 1400 °C under 10 ppm oxygen (balance inert). Results for $La_{1-x}Sr_xMnO_{3-\delta}$ are computed based on the thermogravimetric data reported by Misuzaki *et al.*[19,20,25] Behavior is compared to that of $CeO_{2-\delta}$, computed based on the thermodynamic data reported by Panlener *et al.*[24] Vertical lines correspond to $\Delta\delta_{max}$ for each composition. Where the curves are shown using dotted lines, the computation has large uncertainty due a gap in the thermogravimetric data in the vicinity of $\delta = 0$.

Figure 11. Λ plotted as function of oxygen partial pressure and strontium content in $La_{1-x}Sr_xMnO_{3-\delta}$. Open circles indicate the value of Λ after quenching from 1400 °C (under 10 ppm oxygen) to 800 °C.

Figure 12. Peak flux of hydrogen plotted against (a) change in oxygen content, and (b) change in chemical potential over the course of the oxidation by 0.2 atm steam (balance inert) at 800 °C after quenching from reduction under 10 ppm O_2 (balance inert) at 1400 °C.

July 3, 2014

Table 1. Cycle-averaged fuel productivity of $La_{1-x}Sr_xMnO_{3-\delta}$. Also reported are the (experimental) measurement time, the measured H_2/O_2 ratio, the projected gas production based on the profile characteristics and a presumed sufficiently long equilibration time, and the estimated time to reach the projected value. In addition, the predicted O_2 release on the basis of the thermodynamic analysis is provided for comparison.

x of $La_{1-x}Sr_xMnO_{3-\delta}$	Measured Gas Production (ml/g)		Measurement time (min)		H_2/O_2 (unitless)	Projected Gas Production (ml/g)		Projection time (min)		Predicted O_2 Release (ml/g)
Gas species	O_2	H_2	O_2	H_2		O_2	H_2	O_2	H_2	
0.1	0.55 ± 0.09	0.91 ± 0.04	12	8	1.64 ± 0.02	0.65 ± 0.12	0.91 ± 0.04	46	8	0.5 ± 0.4
0.2	1.45 ± 0.05	2.89 ± 0.07	45	16	2.00 ± 0.04	1.53 ± 0.04	2.89 ± 0.07	91	22	0.9 ± 0.3
0.3	3.4 ± 0.3	5.68 ± 0.07	60	31	1.68 ± 0.05	3.8 ± 0.3	6.26 ± 0.09	177	92	3.3 ± 0.2
0.4	4.9 ± 0.4	8.9 ± 0.2	70	60	1.84 ± 0.03	5.3 ± 0.5	10.3 ± 0.4	192	210	6.1 ± 0.8

July 3, 2014

J. Mater. Chem. A

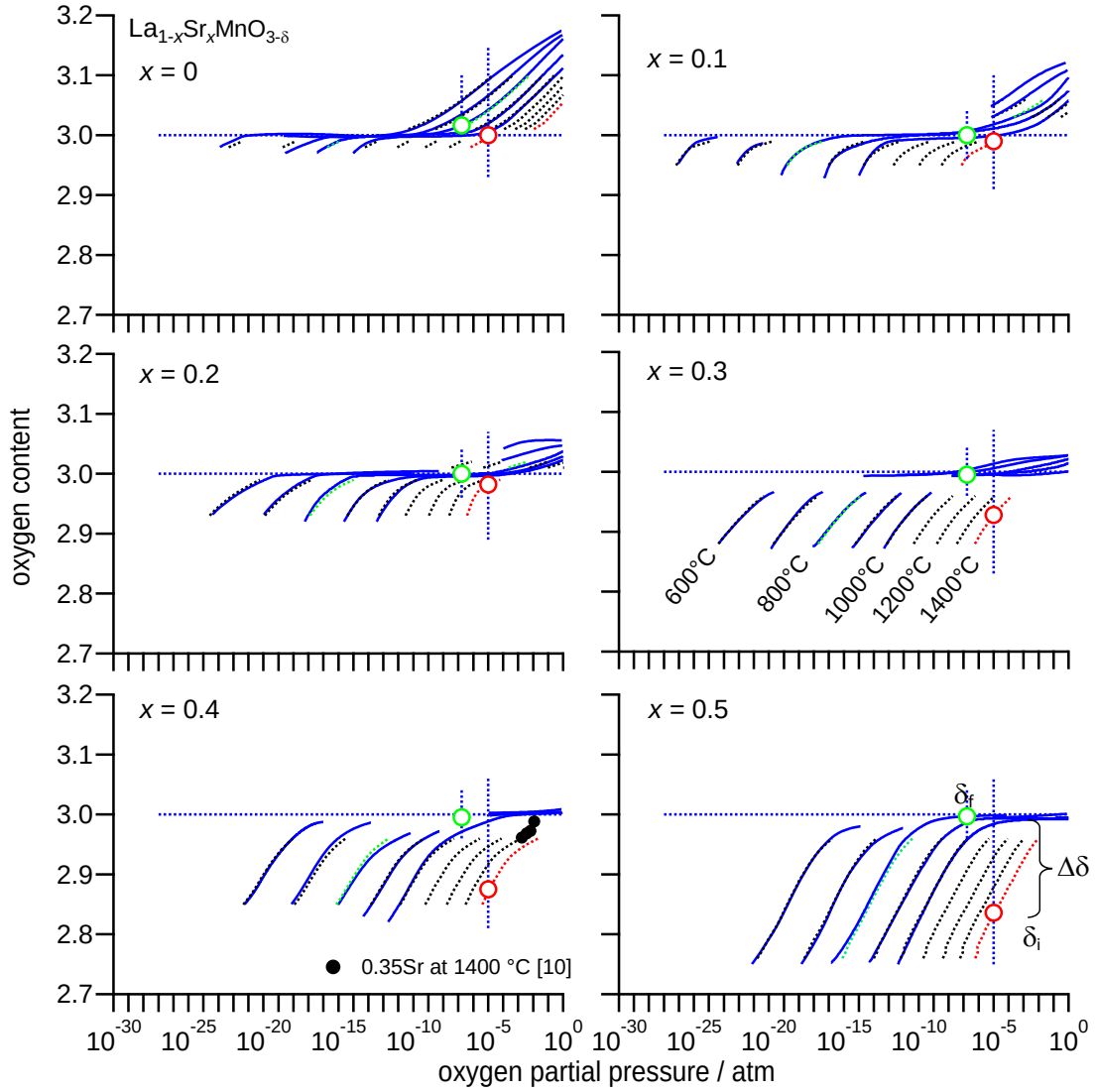

Figure 1. Oxygen content in $La_{1-x}Sr_xMnO_{3-\delta}$ for several different values of x, as indicated. Solid blue lines are the experimental data for Mizusaki and co-workers,[22,23,28] collected for the temperature range from 600 to 1000 °C. High temperature experimental data for the $x = 0.35$ composition[10] are shown on the $x = 0.4$ plot as solid black dots. Dotted lines are fit and/or extrapolated values, derived as described in the text. Red dotted lines refer to extrapolated behavior at 1400 °C, at which reduction was carried in the present thermochemical cycling experiments. Green dotted lines refer to fit data at 800 °C, at which oxidation was performed. Open red and green circles indicate, respectively, expected values of oxygen content upon reduction under 10 ppm O_2 and oxidation under 20% H_2O. The difference in oxygen content between these open circles corresponds to $\Delta\delta_{max}$ shown in Figure 10.

July 3, 2014

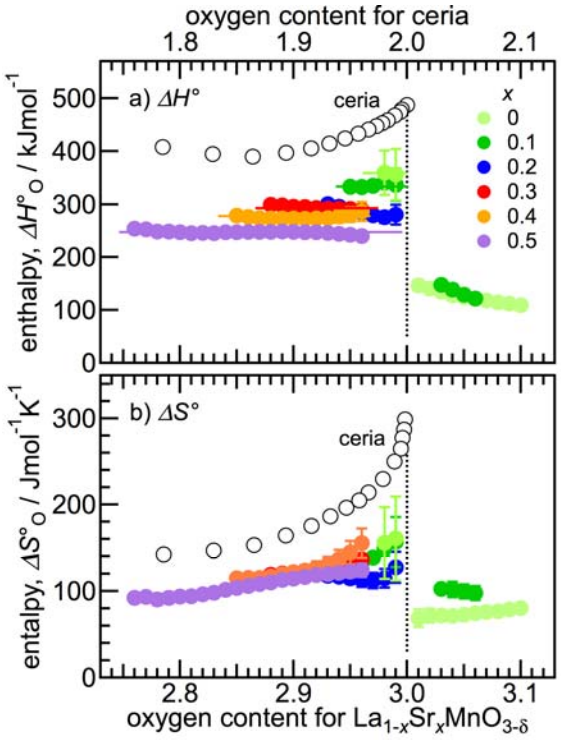

Figure 2. Thermodynamic characteristics of the reduction of $La_{1-x}Sr_xMnO_{3-\delta}$: a) enthalpy and b) entropy of reduction as functions of oxygen non-stoichiometry; data for undoped ceria[27] shown for comparison.

July 3, 2014

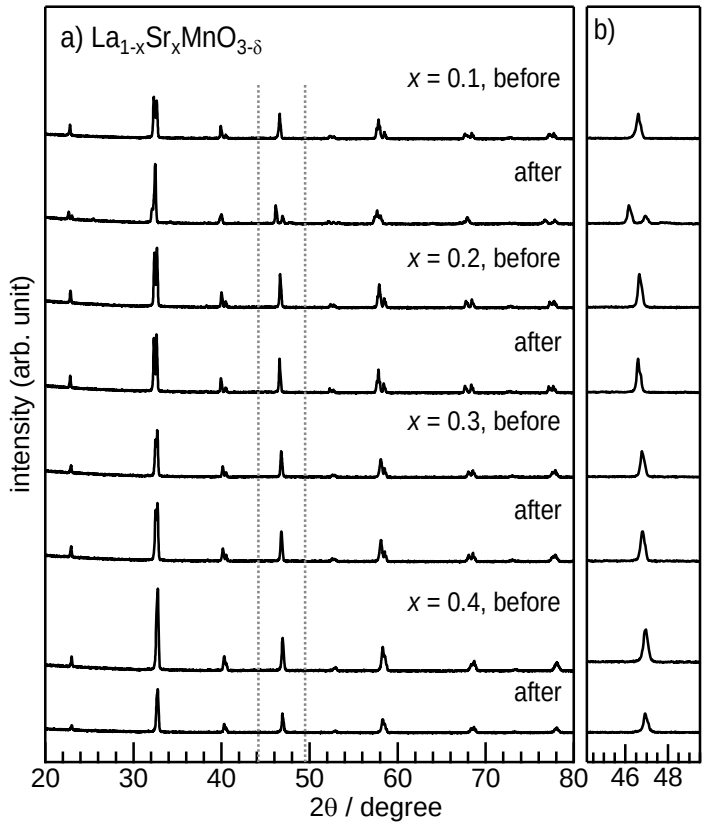

Figure 3. X-ray powder diffraction patterns of $La_{1-x}Sr_xMnO_{3-\delta}$ before and after thermochemical cycling between 800-1400 °C: a) wider range and b) narrower range showing phase change from rhombohedral ($R\bar{3}c$) to orthorhombic (*Pbnm*) in $La_{0.9}Sr_{0.1}MnO_{3-\delta}$ after cycling. Dashed lines in a) indicate the region shown in b).

July 3, 2014

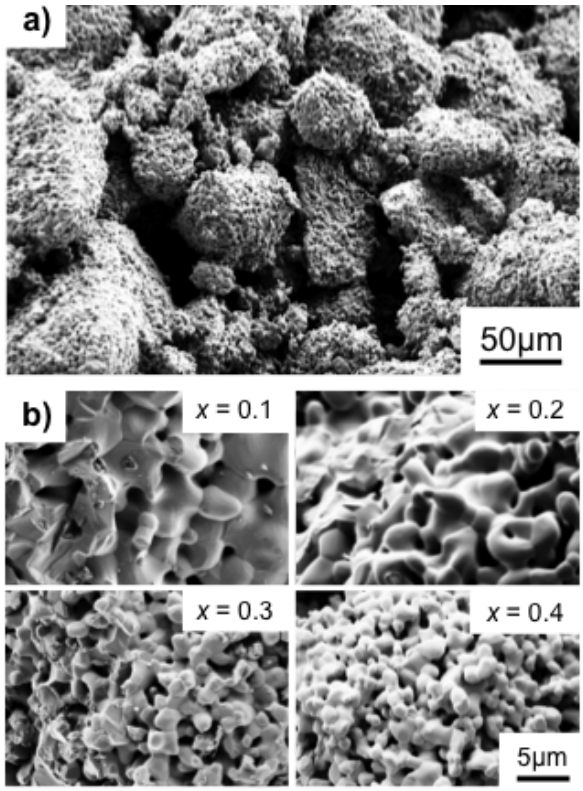

Figure 4. Microstructure of $La_{1-x}Sr_xMnO_{3-\delta}$ before thermochemical cycle between 800-1400 °C: a) typical porous structure for $x = 0.2$, b) impact of strontium content on grain size.

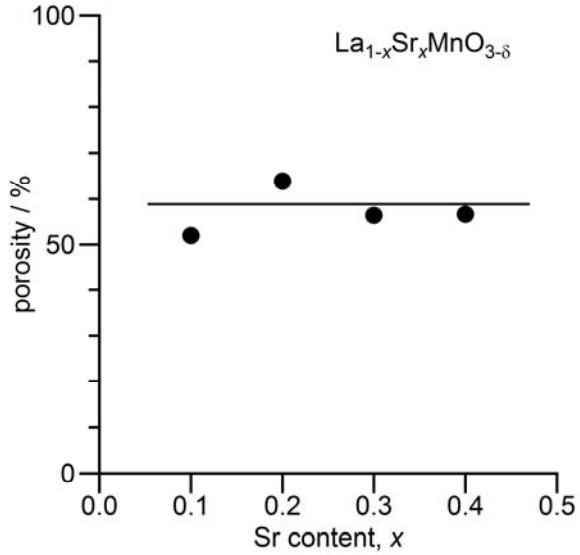

Figure 5. Porosity of $La_{1-x}Sr_xMnO_{3-\delta}$ as a function of strontium content before thermochemical cycle.

July 3, 2014

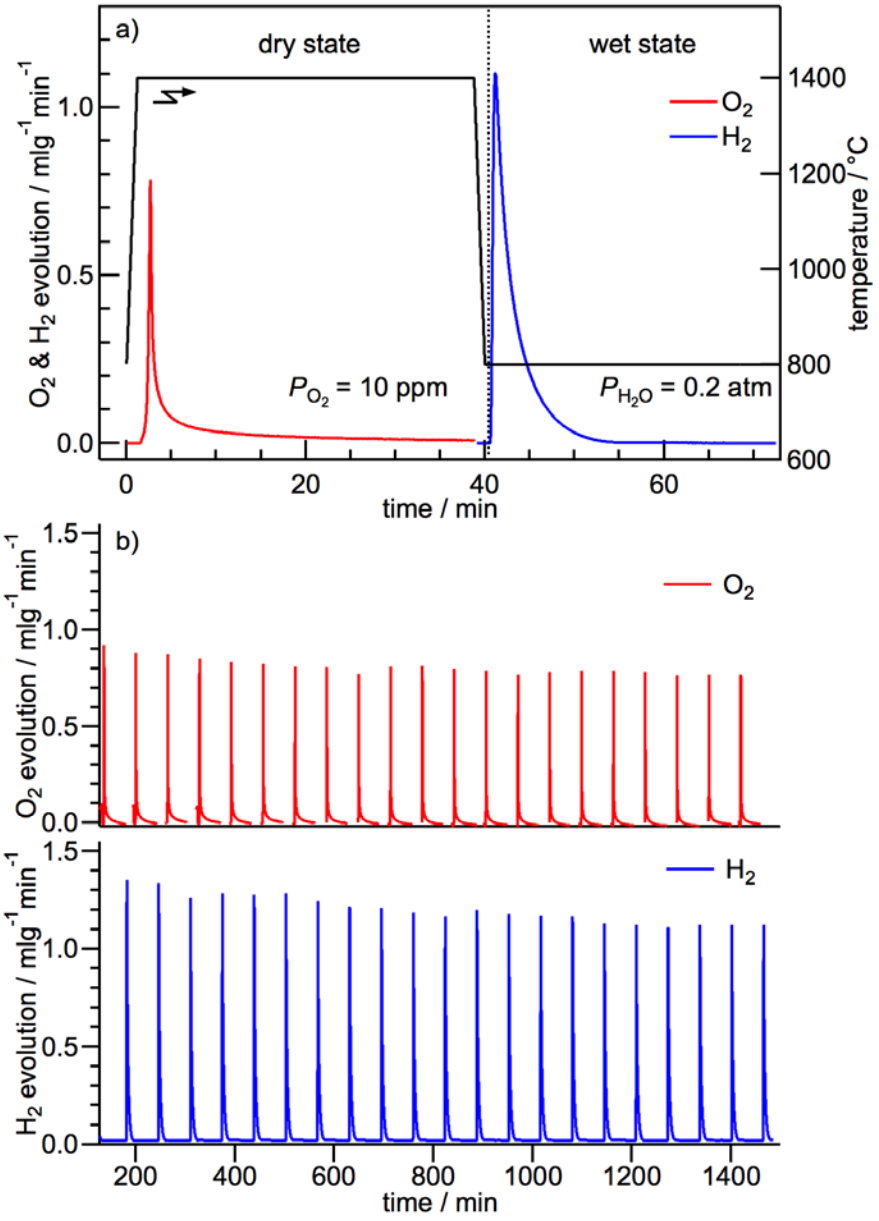

Figure 6. Thermochemical cycle of 1400 – 800 °C using $La_{0.8}Sr_{0.2}MnO_{3-\delta}$: a) typical cycle between high temperature dry state and low temperature wet state for 40 min in each step, b) 21 continuous cycles for thermochemical water splitting. Red and blue colors correspond to oxygen and hydrogen evolution, respectively. The high-temperature reduction and low-temperature oxidation steps were hold for 47 and 16 min, respectively.

July 3, 2014

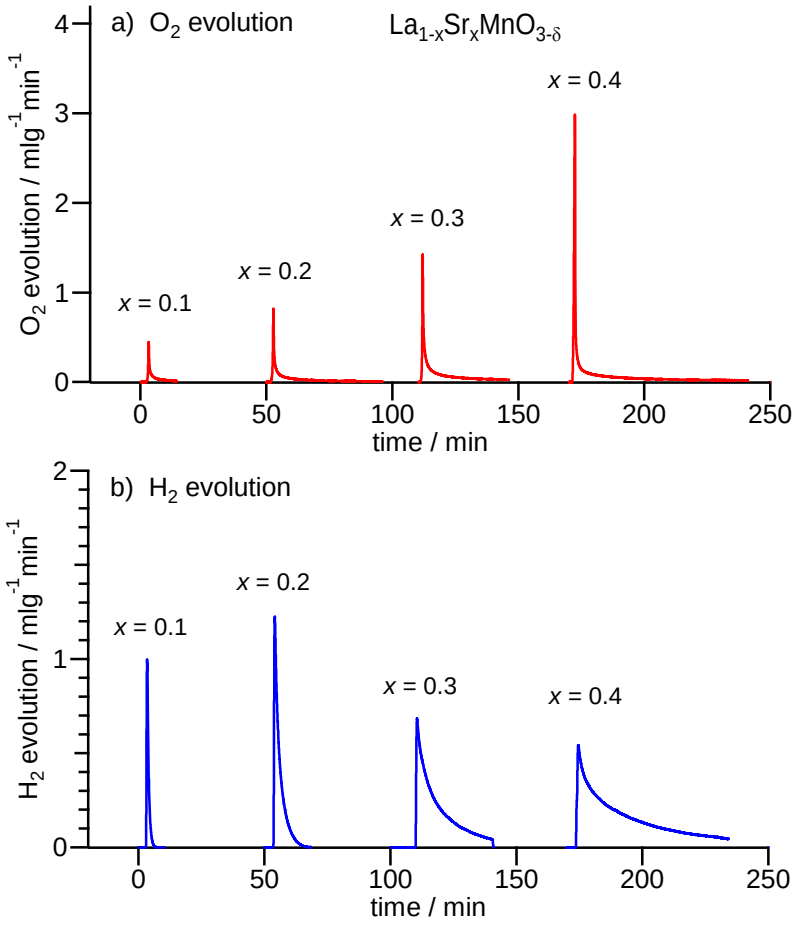

Figure 7. Impact of strontium substitution in $La_{1-x}Sr_xMnO_{3-\delta}$ on thermochemical water splitting during 1400 – 800 °C cycle: a) oxygen evolution at 1400 °C, b) hydrogen evolution at 800 °C. The reduction time for 0.1, 0.2, 0.3 and 0.4 Sr at 1400 °C were 12, 47, 60 and 70 min, respectively, while the oxidation time at 800 °C were 8, 16, 36 and 65 min, respectively.

July 3, 2014

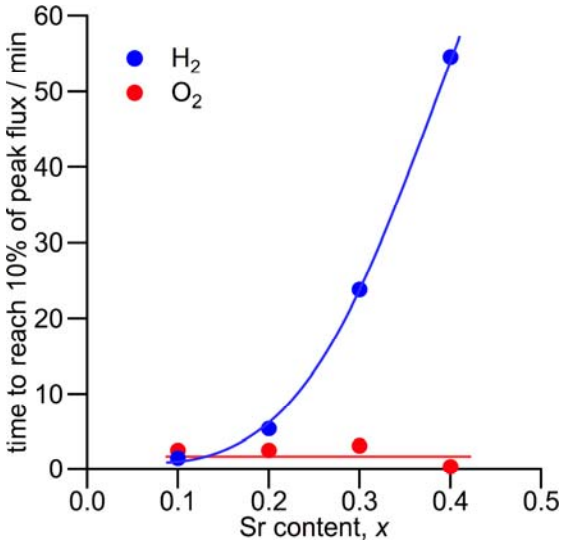

Figure 8. Characteristic hydrogen production and oxygen release times as functions of Sr content. Characteristic time is defined as that required for the off-gas detection to fall to 10% of the peak value.

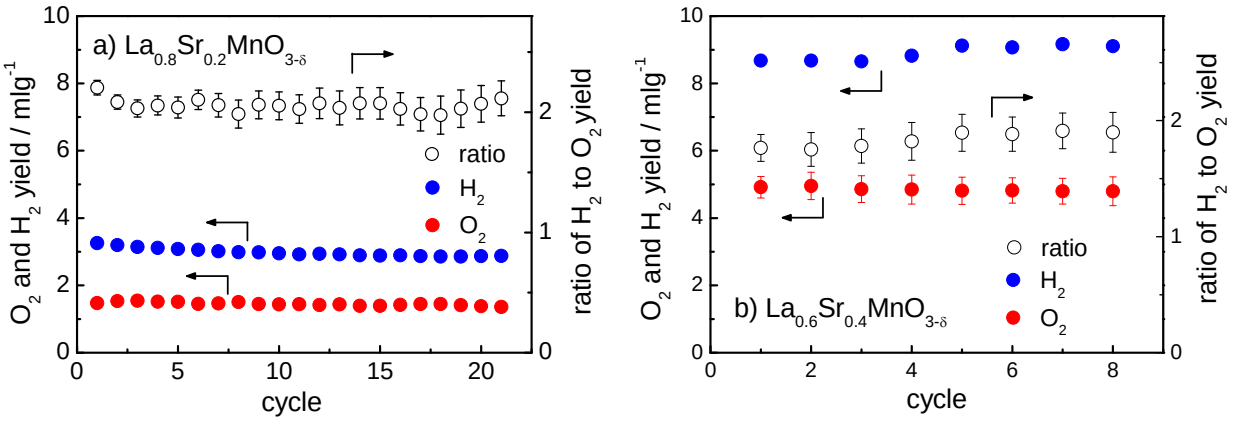

Figure 9. Hydrogen and oxygen yield in $La_{1-x}Sr_xMnO_{3-\delta}$: a) $x = 0.2$ and b) $x = 0.4$. Reproducible hydrogen (blue) and oxygen (red) evolution over 21 and 8 cycles was observed in 0.2 and 0.4 Sr pellets, respectively. The reduction and oxidation times for 0.2 Sr were 47 and 16 min, respectively, whereas those for 0.4 Sr were 70 and 65 min, respectively. Uncertainty is estimated from the signal drift as observed during calibration. Where omitted, error bars lie within the data symbol.

July 3, 2014

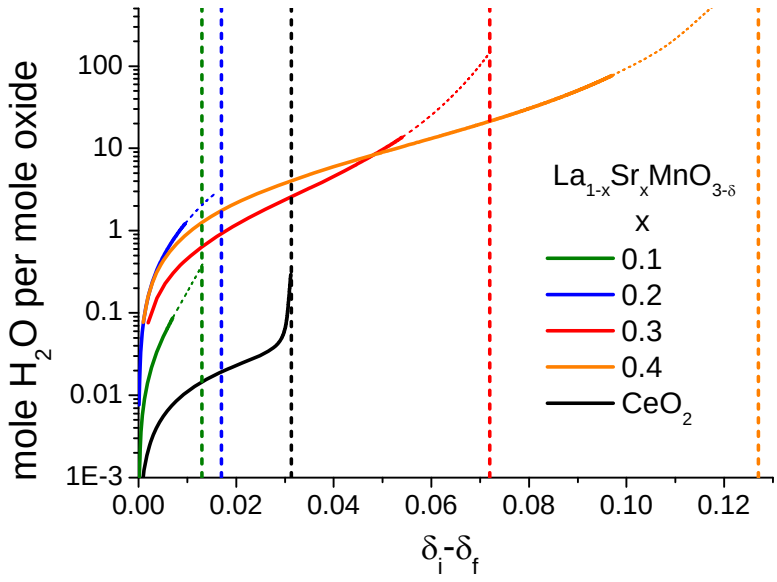

Figure 10. Moles of water vapor required to induce the indicated stoichiometry change per mole of oxide at 800 °C using an input gas stream with pH_2O = 0.2 atm (balance inert), after reduction at 1400 °C under 10 ppm oxygen (balance inert). Results for $La_{1-x}Sr_xMnO_{3-\delta}$ are computed based on the thermogravimetric data reported by Misuzaki *et al.*[19,20,25] Behavior is compared to that of $CeO_{2-\delta}$, computed based on the thermodynamic data reported by Panlener *et al.*[24] Vertical lines correspond to $\Delta\delta_{max}$ for each composition. Where the curves are shown using dotted lines, the computation has large uncertainty due a gap in the thermogravimetric data in the vicinity of $\delta = 0$.

July 3, 2014

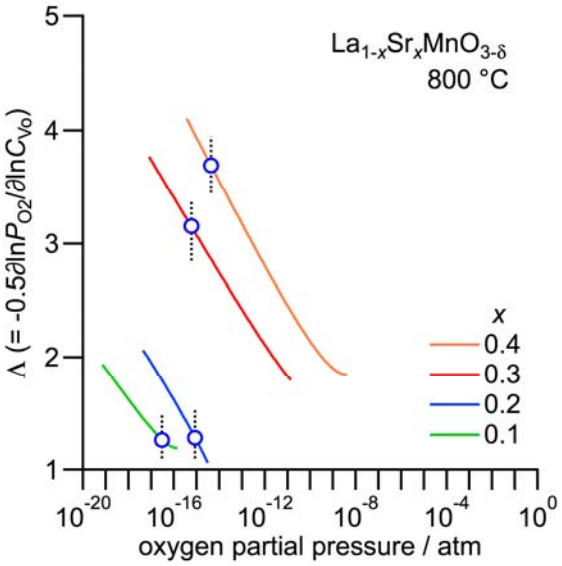

Figure 11. Λ plotted as function of oxygen partial pressure and strontium content in $La_{1-x}Sr_xMnO_{3-\delta}$. Open circles indicate the value of Λ after quenching from 1400 °C (under 10 ppm oxygen) to 800 °C.

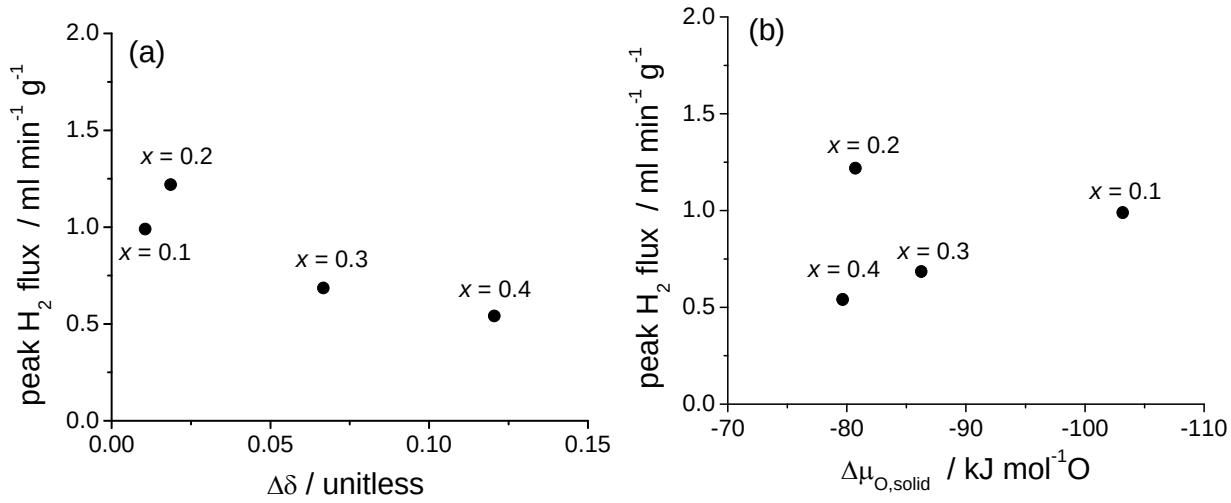

Figure 12. Peak flux of hydrogen plotted against (a) change in oxygen content, and (b) change in chemical potential over the course of the oxidation by 0.2 atm steam (balance inert) at 800 °C after quenching from reduction under 10 ppm O_2 (balance inert) at 1400 °C.